nature materials

ARTICLES

PUBLISHED ONLINE: 13 JUNE 2016 | DOI: 10.1038/NMAT4661

Crystal symmetry breaking and vacancies in colloidal lead chalcogenide quantum dots

Federica Bertolotti[1], Dmitry N. Dirin[2,3], Maria Ibáñez[2,3], Frank Krumeich[2], Antonio Cervellino[4], Ruggero Frison[5,6], Oleksandr Voznyy[7], Edward H. Sargent[7], Maksym V. Kovalenko[2,3], Antonietta Guagliardi[6]* and Norberto Masciocchi[1]*

Size and shape tunability and low-cost solution processability make colloidal lead chalcogenide quantum dots (QDs) an emerging class of building blocks for innovative photovoltaic, thermoelectric and optoelectronic devices. Lead chalcogenide QDs are known to crystallize in the rock-salt structure, although with very different atomic order and stoichiometry in the core and surface regions; however, there exists no convincing prior identification of how extreme downsizing and surface-induced ligand effects influence structural distortion. Using forefront X-ray scattering techniques and density functional theory calculations, here we have identified that, at sizes below 8 nm, PbS and PbSe QDs undergo a lattice distortion with displacement of the Pb sublattice, driven by ligand-induced tensile strain. The resulting permanent electric dipoles may have implications on the oriented attachment of these QDs. Evidence is found for a Pb-deficient core and, in the as-synthesized QDs, for a rhombic dodecahedral shape with nonpolar {110} facets. On varying the nature of the surface ligands, differences in lattice strains are found.

Colloidal semiconductor nanocrystals, also known as quantum dots (QDs) owing to their strong quantum-size effects, are an important class of building blocks for electronic, optoelectronic and thermoelectric devices[1,2]. Owing to their exceptional size- and shape-tunable optical and electronic properties, as well as their low-cost solution processability, lead chalcogenide (PbE, E = S, Se, Te) QDs have attracted a great deal of attention at an increasing pace in the past 25 years, and a number of solid-state device applications (such as diode lasers, infrared detectors and solar cells) are being pursued at present[3–5]. In PbE QDs, the electronic and optical characteristics are strongly influenced by the structure and stoichiometry of the nanocrystals, both at their interior and at their surface. These species crystallize in the highly symmetric rock-salt crystal structure; a metastable rhombohedral phase (of the α-GeTe type) has been theoretically predicted for bulk PbS[6] and temperature-dependent cation disordering has been reported for bulk PbS and PbTe, with no macroscopic crystal symmetry change[7,8]. For nanometre-sized QDs, lattice and structural distortions induced by the extreme downsizing of the nanocrystals, by their morphology and/or by surface-induced ligand effects, have not been detected so far. Concerning stoichiometry, colloidal synthesis typically provides metal-rich PbE QDs, with a larger metal excess for smaller sizes and with anionic ligands preserving charge neutrality[9,10]. There exists a general consensus that nanocrystals possess a stoichiometric core whereas the excess metal cations form a labile surface layer. This external layer reversibly dissociates from, and binds to, the crystal surface in the form of metal–ligand complexes, resulting in dynamic chemical formulae, surface reconstruction phenomena and QD size reduction over time[11,12]. All these effects strongly influence the reactivity and optoelectronic properties of the QDs. Therefore, controlling the stoichiometry of the QDs is of utmost importance for understanding the relationship between their properties and structure[13]. However, the facile adsorption and desorption of metal complexes at the nanocrystal surface make the accurate description of QD stoichiometry a challenging task for standard analytical methods.

Using X-ray total scattering techniques on colloidal organic oleate(OA)-capped PbS and PbSe QD solutions and a model based on the Debye scattering equation (DSE)[14], we experimentally unveil the distortion of the rock-salt structure towards a non-centrosymmetric rhombohedral ($R3m$) structure, due to the displacement of the Pb sublattice along the [111] axis (Fig. 1a). This distortion is confirmed using density functional theory (DFT) calculations and is probably triggered by the stereochemical effect of the $6s^2$ lone pair of Pb(II) ions[6], favoured by ligand-induced tensile stress in spherical nanoparticles. Our analysis also provides strong evidence of an unexpected compositional picture of such QDs: a Pb-deficient core and a Pb-enriched shell within a homo-core-shell model.

The rock-salt structure of PbE nanocrystals in the conventional face-centred cubic lattice is shown in Fig. 1a; the face-centred cubic lattice is equally well described by the primitive rhombohedral unit cell emphasized by the shaded boundaries in Fig. 1a, and characterized by the interaxial angle α_{RH}. This primitive unit cell is here used to describe both the pristine cubic lattice ($\alpha_{RH} = 60°$) and the rhombohedrally distorted lattice resulting from a tensile ($\alpha_{RH} < 60°$) deformation along the [111] direction.

Highly monodisperse PbS and PbSe QDs were analysed by generating atomistic models of spherical homo-core-shell

[1]Dipartimento di Scienza e Alta Tecnologia and To.Sca.Lab, Università dell'Insubria, via Valleggio 11, I-22100 Como, Italy. [2]Department of Chemistry and Applied Biosciences, ETH, Vladimir-Prelog-Weg 1, CH-8093 Zürich, Switzerland. [3]Empa-Swiss Federal Laboratories for Materials Science and Technology, Überlandstrasse 129, CH-8600 Dübendorf, Switzerland. [4]SLS, Laboratory for Synchrotron Radiation—Condensed Matter, Paul Scherrer Institut, CH-5232 Villigen, Switzerland. [5]Department of Chemistry, University of Zürich, Winterthurerstrasse 190, CH-8057 Zürich, Switzerland. [6]Istituto di Cristallografia and To.Sca.Lab, CNR, via Valleggio 11, I-22100 Como, Italy. [7]The Edward S. Rogers Department of Electrical and Computer Engineering, University of Toronto, 10 King's College Road, Toronto, Ontario M5S 3G4, Canada. *e-mail: antonella.guagliardi@ic.cnr.it; norberto.masciocchi@uninsubria.it

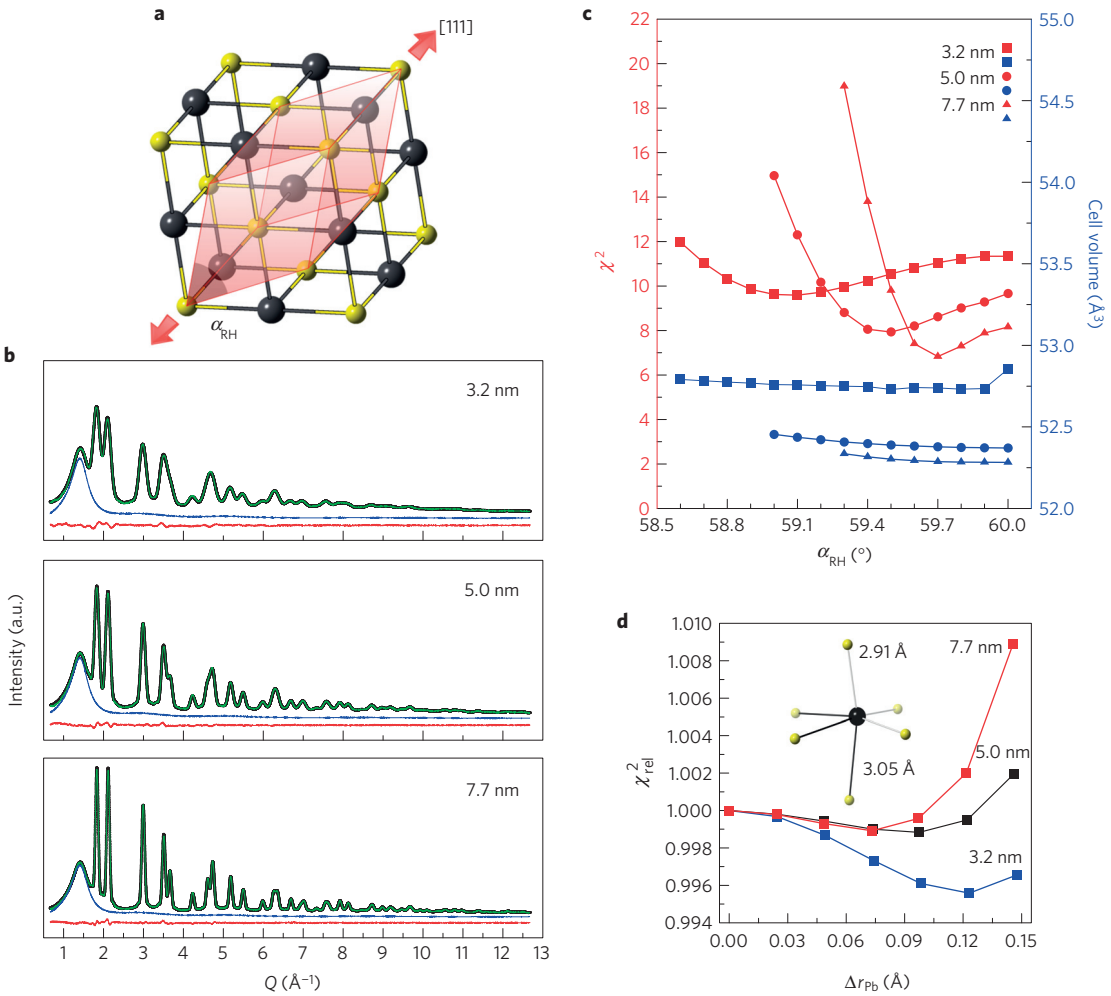

Figure 1 | Lattice distortion of the rock-salt structure in PbS QDs. a, Rock-salt structure of PbS with the primitive rhombohedral unit cell (shaded area). Tensile deformations of the cubic structure along the [111] direction (arrows) induce a contraction of the rhombohedral angle α_{RH} to values smaller than 60°. **b**, Experimental synchrotron X-ray diffraction data of colloidal PbS QDs (black trace) in hexane (blue trace) with the Debye total scattering (texture-free) pattern model superimposed as a green line and the difference curve (red trace), at the bottom of each plot. **c**, Reduced χ^2 for the best fit of the DSE models to each set of data at different α_{RH} angles, with the corresponding cell volume variation. **d**, χ^2_{rel} versus Δr_{Pb}, the offset of the Pb atom along [111], from the rock-salt position [$\chi^2_{rel} = \chi^2(\Delta r_{Pb})/\chi^2(0)$], for the three different sizes: 7.7 nm (red), 5.0 nm (black) and 3.2 nm (blue). We notice that the Pb offset follows the deviation of the α_{RH} from 60° (the larger the shift, the larger the deviation). The inset in **d** shows the distortion of the PbS_6 octahedra resulting in three shorter (2.91 Å) and three longer (3.05 Å) Pb-S distances breaking the centrosymmetry of the rock-salt structure. In **a** and in the inset of **d**, colours of atomic species represent: black, lead; yellow, sulfur. In **c** and **d**, solid lines represent guides for the eye.

nanocrystals, with adjustable core diameter, shell thickness, lattice parameter and stoichiometry, and also by using an innovative DSE approach[14] to simulate the reciprocal space scattering pattern while optimizing the model parameters to fit the experimental data. For PbS, the analysis was performed on both freshly prepared samples and their aged counterparts after partial oxidation by storage at ambient conditions.

With respect to the structural reordering in very small QDs, PbS and PbSe are found to be very similar; herein we focus on the case of PbS, considering three different sizes (3.2, 5.0 and 7.7 nm). Outcomes for PbSe are provided in the Supplementary Information.

The main results concerning rhombohedrally distorted model(s) of as-synthesized PbS QDs are summarized in Fig. 1b–d. By lowering the α_{RH} angle from 60° to 58.6°, we investigated competing structural models for each of the three samples. The reduced χ^2 (goodness of fit) of each model is given in Fig. 1c as a function of α_{RH} and clearly indicates that the best agreement is obtained for α_{RH} values <60° (Fig. 1b and Supplementary Figs 2–4). The rhombohedral lattice distortion (confirmed by conventional Rietveld analysis, see Supplementary Fig. 30) varies in inverse proportion with size. The shallowest minimum (at 59.1°) is observed for the smallest size (3.2 nm) QDs, with deeper minima (at 59.5° and 59.7°) for the 5.0 and 7.7 nm QDs, respectively, in agreement with the smearing effect of the reduced nanocrystal coherent domains.

In our search for the driving force inducing such lattice distortion, we observed a similar size dependence for the cell volume variation (Fig. 1c). The volume expansion of the unit cell at the smallest size is fairly large (>1.1%) compared, for example, to the volume increase in GeTe, a mere 0.8% for a temperature variation of 400 °C (ref. 15). The inverse relationship between the cubic-equivalent lattice parameter ($V_{cell}^{1/3}$) and QD diameter D (Fig. 2a) provides a $V_{cell}^{1/3}$ slightly smaller than the value of bulk galena, when extrapolated to large sizes, and a negative surface tension value ($\gamma = -3.86\,eV\,nm^{-2}$). According to a previous prediction[6], the negative pressure induces a tensile stress, enabling the shift of Pb atoms along the [111] direction, (prompted by the incipient stereochemical activity of the Pb(II) $6s^2$ lone pair[6]), which causes the lattice distortion. Therefore, different Pb-sublattice displacements

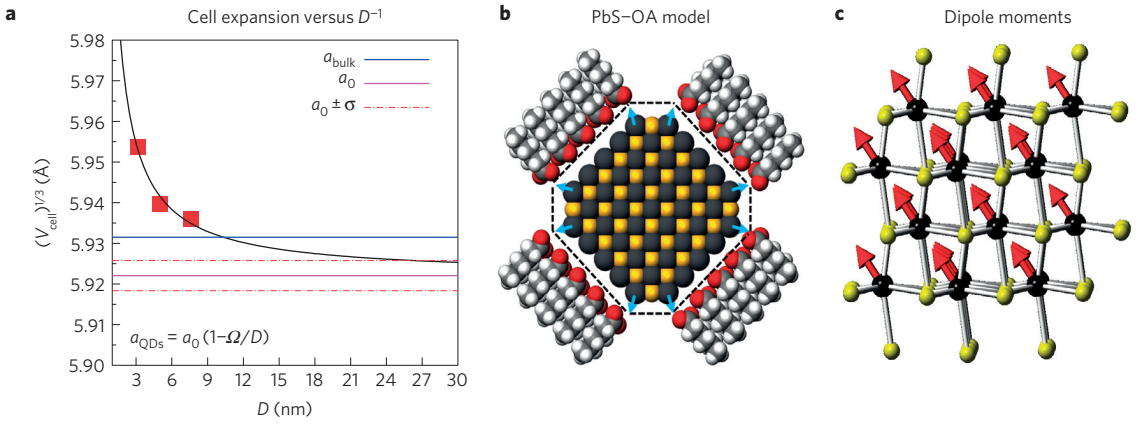

Figure 2 | Size-dependent lattice expansion, ligands-induced tensile stress and dipole moment. a, Dependence of the cubic-equivalent lattice parameter $(V_{cell})^{1/3}$ on the nanocrystal diameter (D) for PbS QDs. $(V_{cell})^{1/3}$ expands on decreasing the QD size (red points). The solid black curve is obtained by fitting the $(V_{cell})^{1/3}$ values with an inverse dependence law on the sample diameter: $a_{QDs} = a_0\,(1-\Omega/D)$, where $\Omega = 4\gamma/3B$ depends on the surface tension (γ) and on the bulk modulus (B), and a_0 is the lattice parameter for $D \to \infty$ (approaching the bulk value a_{bulk}). We obtained $\gamma = -3.86\,\mathrm{eV\,nm^{-2}}$, indicating a negative surface tension responsible for the observed lattice expansion. **b**, Schematic of a tensile surface stress arising from inter-ligand distances larger than the spacing between {110} surface adsorption sites; the view shows a thin (001) cut, horizontal and vertical axes are [100] and [010], respectively. **c**, PbS rhombohedrally distorted structure viewed along [01$\bar{1}$], with the dipole vectors (red arrows) originating from the shift of the Pb ions (augmented for graphical clarity) and the loss of centrosymmetry. A net dipole moment $\mu = 190D$ is estimated for the 3.2 nm QDs. In **b** and **c**, colours of atomic species represent: black, lead; yellow, sulfur; red, oxygen; grey, carbon; white, hydrogen.

were investigated at the optimal α_{RH} angle and the relative change of χ^2 is shown in Fig. 1d. The displacement observed in our PbS QDs is minimal compared to that predicted for the bulk material[6], although in line with other estimates[7,8], and correlates well with the amount of lattice distortion. The Pb shift causes three shorter and three longer Pb-S distances to arise (2.91 Å and 3.05 Å for the smallest QDs), providing a (3 + 3) coordination of Pb by S, and the loss of centrosymmetry in the structure. DFT calculations performed on bulk PbS confirmed such ferroelectric-type structural distortion under the effect of a hydrostatic tensile stress. In nanocrystals, such tensile stress could be induced by ligands whose packing density is not commensurate with the underlying adsorption sites[16] (Fig. 2b). Reproducing the ensuing structural distortion of the nanocrystals computationally is more difficult owing to the unknown surface structure and ligands organization (Supplementary Fig. 29).

An important consequence of such a ferroelectric-type structural distortion is the formation of a permanent electric dipole along [111], which may play a plausible role in the observed spontaneous linear aggregation of PbE QDs into wire-like structures in suspension and in dipole-driven co-alignment in oriented attachment phenomena[17,18]. Calculations on the unrelaxed experimentally determined 3.2 nm PbS QD structure with Pb-sublattice shift produce a large dipole moment $\mu \approx 190$ D (Fig. 2c); estimates for spherical PbSe are plausible in line with experimental reports[18] (see the Supplementary Information). The current literature attributes the dipole-driven oriented attachment of PbE QDs to asymmetries in Pb- and E-terminated polar {111} facets[17], despite that the presence of unpassivated E-rich facets conflicts with the established consensus that nanocrystals are Pb-terminated. Therefore, characterizing the morphology of these QDs becomes of greatest importance. PbS QDs have been reported to show cubic and cuboctahedral shapes, with a subtle interplay of {100} and {111} forms[19]. {110} facets are reported to appear at the initial stages of nanocrystal formation and, being highly reactive, to be preferentially consumed during growth[17,20] (the disposition of the three types of facets is given in the inset of Fig. 3b). Unambiguously determining the shape of QDs in this work by direct imaging remained challenging, as most nanocrystals appeared roundish. DSE modelling of the small angle X-ray scattering (SAXS) signal of PbS colloids (in the Porod's region, sensitive to the local interface roughness) provides evidence for a rhombic dodecahedral morphology in the as-synthesized suspensions (Fig. 3a and Supplementary Figs 11 and 12). This morphology is further supported by X-ray powder diffractometry on dried samples. Similarly to other reports for Cu_2O nanocrystals[21], diffraction data (Fig. 3c,d and Supplementary Fig. 14) show a significantly enhanced intensity of the 220 peak. The cubic harmonics description of textural effects in a conventional Rietveld fit provided the three-dimensional (3D) shapes of the relative orientation distribution function (ODF) (Fig. 3c,d insets); the results indicate a nonrandomness of the QD orientation with preferential alignment of their (110) planes as parallel to the substrate. The implicit relation between the symmetry-related preferred orientation poles (indicated by 12 arrows) and the underlying rhombic dodecahedral nanocrystal shape is shown in Fig. 3g. Selected high-angle annular dark-field (HAADF-STEM) (Fig. 4a,b) and phase contrast scanning transmission electron microscopy (PC-STEM) (Fig. 4c) images also suggest that the habit of nanoparticles can very closely approximate that of a rhombic dodecahedron. A recent high-resolution TEM (HRTEM) and Fourier analysis study of the orientational relationship of oleic acid-stabilized PbS QDs forming 2D superlattices showed that the large majority of nanoparticles (>70%) possess a [110] orientation, although a truncated octahedral shape was proposed[22]. All these findings indicate that the rhombic dodecahedron is the dominant morphology in as-synthesized PbS QDs; the nonpolar nature of {110} forms dismisses the hypothesis of asymmetries in the faceting of nanocrystals, making the ferroelectric-type structural distortion a plausible cause for the formation of a dipolar moment.

On oxidation, a less pronounced ODF isosurface is found (Fig. 3e,f), which is consistent with the presence of rhombicuboctahedral clusters bound by polar {111} and nonpolar {100} and {110} facets[23] (appearing as red, blue and green coloured facets, respectively, in Fig. 3h). The SAXS-DSE simulations (Fig. 3b) support such a morphological change. These findings suggest that the initially formed rhombic dodecahedral shape (possessing {110} facets of relatively high surface tension[24]) progressively evolves into more stable forms[25]. Despite the fact that PbS QDs undergo surface reconstruction, they maintain the original ferroelectric-type structural distortion. The simultaneous appearance of {100} and

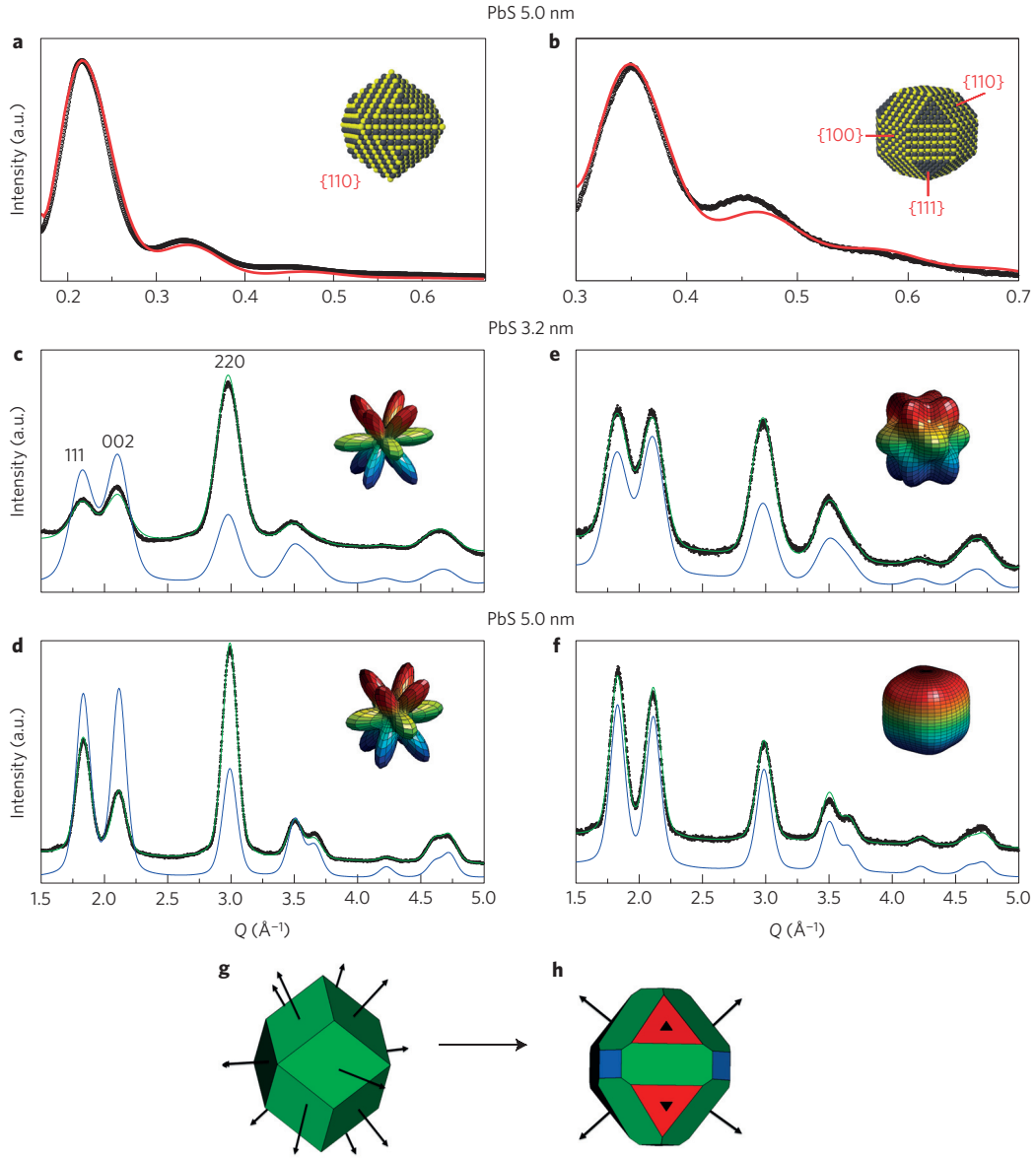

Figure 3 | Morphology evolution of PbS QDs. a,**b**, SAXS signal (black trace) of freshly prepared (**a**) and aged (**b**) PbS 5.0 nm QDs, with the DSE simulation (red trace). The insets show the nanocrystal morphology: rhombic dodecahedral (exposing only {110} facets) and rhombicuboctahedral (exposing also {111} and {100} facets), respectively. Colours of atomic species represent: black, lead; yellow, sulfur. **c**,**d**, X-ray powder diffraction data of dried samples measured in flat-plate geometry (black trace), showing the strong texture along the (220) planes for the freshly prepared 3.2 and 5.0 nm QDs. The green line describes the Rietveld fit correcting the texture effects, the underlying blue line describes the simulated diffraction trace of randomly oriented QDs. The 3D isosurfaces (insets), describing the orientation distribution functions, indicate the nonrandomness of the nanocrystal orientation, with their (110) planes parallel to the substrate. **e**,**f**, X-ray powder diffraction data showing that the effect of preferred orientation fades on sample ageing with increasing 111 and 200 peak intensities. **g**,**h**, Geometric relation between the preferred orientation poles and the underlying rhombic dodecahedral (**g**) or rhombicuboctahedral (**h**) shape. Black arrows represent the directions perpendicular to the nanocrystal facets parallel to the preferred orientation poles.

(asymmetrically distributed) polar {111} facets provide additional weaker dipolar effects (Supplementary Fig. 25), which are however insufficient to explain the experimentally reported values[18,25]. Considering the intricate interplay between the dipolar forces of different origin and other short-range interactions, it is not possible to provide definitive proof that an internal dipole is the primary causative agent in the observed 1D and 2D attachment of PbE nanocrystals of larger sizes and different morphology[17,18,23,26].

However, whether the rhombohedral distortion in spherical-like OA-capped QDs and the Pb off-centring are further due to the extreme downsizing of the PbE nanocrystals cannot be ruled out. Disentangling size from ligand-induced effects would require studying QDs with much shorter carboxylates, or even uncapped ones, which are unavailable as stable colloids with reasonable control over size and size distribution. Nevertheless, when we moved to inorganic ligands[27] via solution exchange of the long-chain oleates with short PbI_3^- or AsS_4^{3-} fragments in PbS QDs, we observed markedly different effects on the X-ray scattering patterns (Fig. 5a). The splitting of *h*00 Bragg peaks in iodoplumbate-capped QDs is neither compatible with the undistorted cubic rock-salt structure nor with its rhombohedral distortion; therefore, a different kind of structural defectiveness, possibly driven by a more complex surface rearrangement, must be considered[28] (see Supplementary Information and Supplementary Figs 31 and 32). The sharpening of

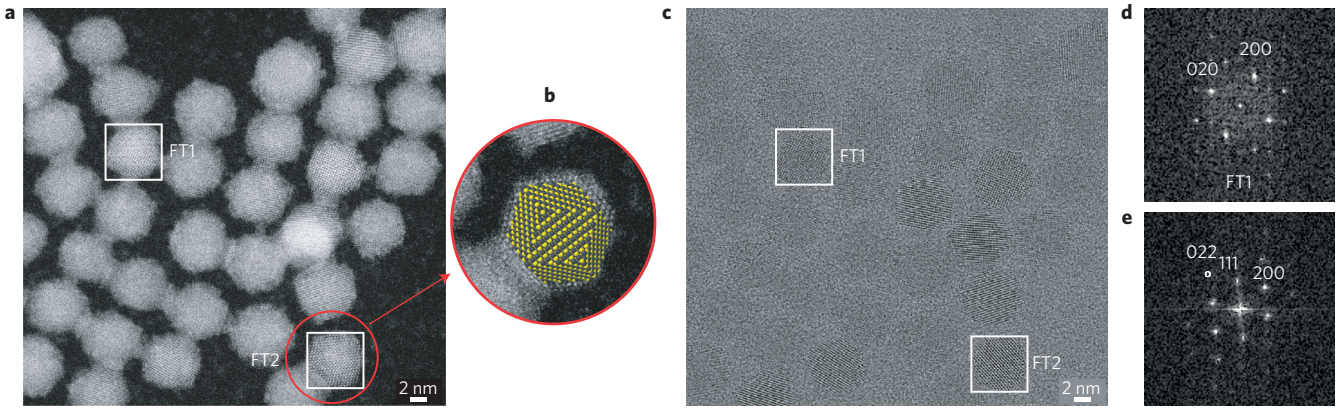

Figure 4 | STEM analysis of the PbS QD structure and morphology. a,**b**, Spherical aberration-corrected HAADF-STEM image of the 7.7 nm sample (**a**) showing that the habit of the nanoparticles can very closely approximate a rhombic dodecahedron (**b**). Here the colours of atomic species represent: black, lead; yellow, sulfur. **c**, High-resolution phase contrast STEM image. **d**,**e**, Fourier transform of the highlighted regions in **c** shows the four-fold and two-fold symmetry of crystals viewed along [001] (**d**) and [110] (**e**).

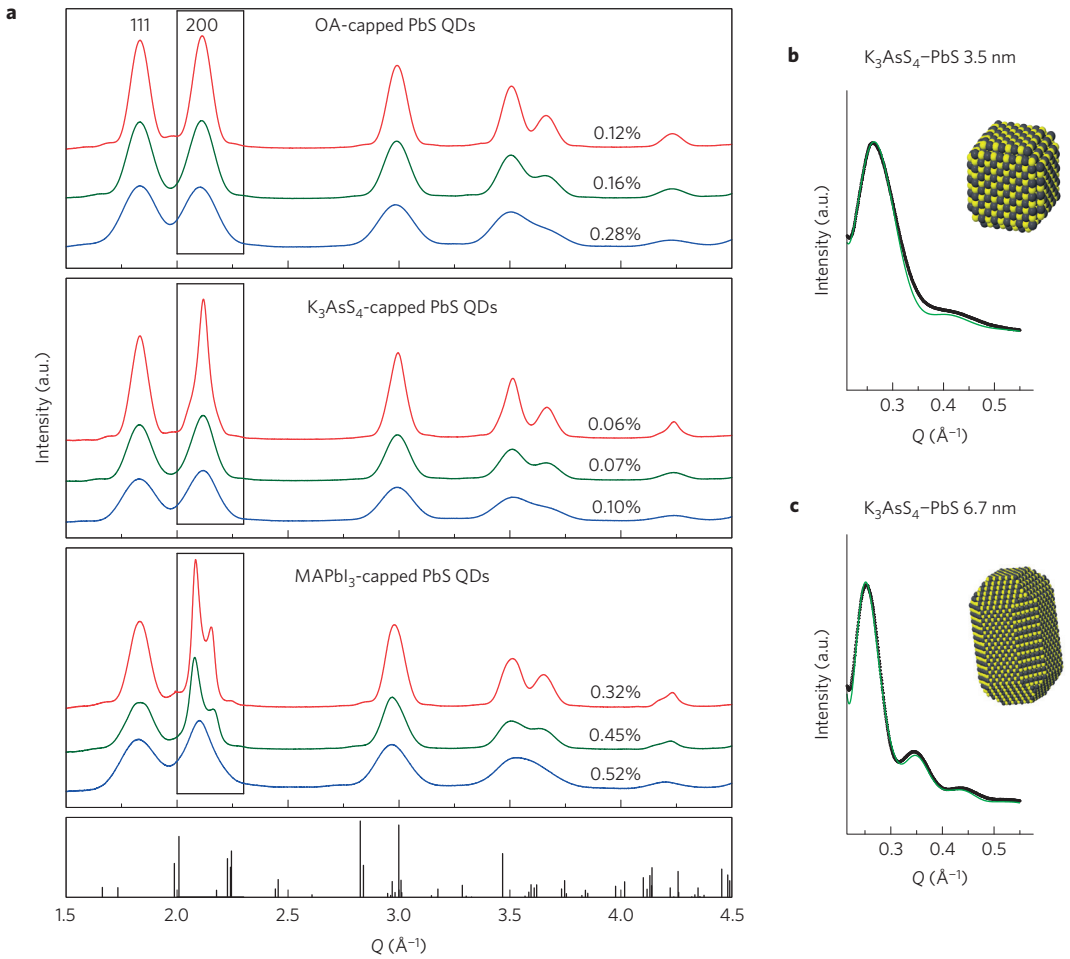

Figure 5 | Organic-to-inorganic ligand exchange and induced lattice strain. a, Experimental synchrotron X-ray diffraction data (subtracted of the solvent signal) collected on pristine OA-capped 3.5, 5.0 and 6.7 nm (blue, green, red traces) PbS colloids (top) and after ligand exchange with inorganic K_3AsS_4 (intermediate) and $MAPbI_3$ (bottom) ligands. The black rectangle highlights the highly reproducible splitting in $MAPbI_3$-capped QDs of the 200 peak (less evident, but fully observable also in the 400 one), which is compatible neither with the undistorted rock-salt structure nor with its rhombohedral distortion. The sharpening of the same *h*00 peaks, for both inorganic ligands, suggest the morphological elongation of nanocrystals parallel to the [100] direction. The narrow peaks in the $MAPbI_3$ case cannot be attributed to contamination by the $MAPbI_3$ phase (Bragg peak positions and intensities are shown for reference). Values in % refer to $\Delta a/a_{bulk}$ and indicate that the three ligands induce a different lattice strain. **b**,**c**, SAXS signal (black trace) of the K_3AsS_4-capped 3.5 nm (**b**) and 6.7 nm (**c**) PbS QDs, with the DSE simulation (green trace). The insets show the nanocrystal morphology: cubic-like (exposing extended {100} facets) in **b** and prismatic-like (originating from the fusion of two pristine clusters), in **c**. Colours of atomic species represent: black, lead; yellow, sulfur.

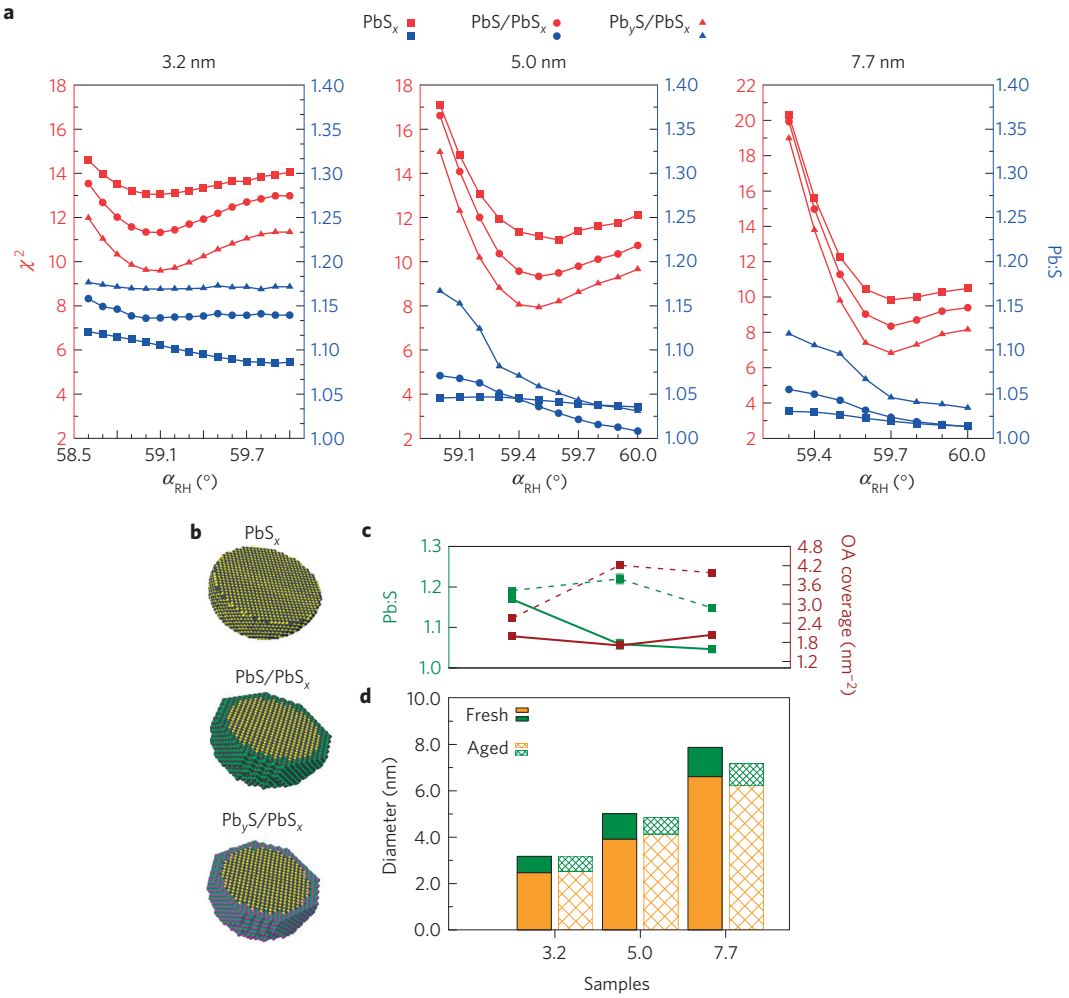

Figure 6 | Stoichiometry of homo-core-shell PbS QDs. a, Reduced χ^2 for the best fit of the DSE models to each set of data at different α_{RH} angles. Each χ^2 curve (red lines) corresponds to a different stoichiometry model and Pb:S ratio (blue lines): PbS_x model ($0 \leq x \leq 1$) with S vacancies throughout the entire QD volume; PbS/PbS_x stoichiometric/non-stoichiometric core-shell model; and Pb_yS/PbS_x core-shell model with a non-stoichiometric core ($0 \leq y \leq 1$) and a non-stoichiometric shell ($0 \leq x \leq 1$). **b**, Graphical view of PbS_x (black, lead; yellow, sulfur), PbS/PbS_x (black, lead; yellow, sulfur core; green, sulfur shell) and Pb_yS/PbS_x (black, lead core; yellow, sulfur core; purple, lead shell; green, sulfur shell) atomistic models. **c**, Pb:S ratio and OA coverage of freshly prepared (solid line) and aged (dashed line) QDs. **d**, QD overall diameter, resulting from the core size (orange) and the shell thickness (green) of the Pb_yS/PbS_x model, for as-synthesized and oxidized samples. In **a** and **c**, solid lines represent guides for the eye.

the *h*00 peaks in both $MAPbI_3$- and K_3AsS_4-capped QDs suggests that some morphological transformations also took place. On top of this, the two inorganic ligands provide markedly different lattice strain (Fig. 5a and Supplementary Fig. 33). Thioarsenates, geometrically more adaptable to the QD surface, show tiny expansions compared to the bulk lattice, with a negligible size dependence, whereas iodoplumbates exhibit lattice expansions even larger than in oleates. These experimental observations indicate that the nature of the ligands does indeed play a remarkable role in modifying the lattice strain. Further analysis of the *h*00 peaks of the largest K_3AsS_4-capped PbS QDs suggests the formation of elongated nanocrystals, the size along the [100] direction being about twice as large as the diameter of the pristine OA-capped QDs. This finding suggests that they are formed by the fusion, in solution, through the {100} facets of two pristine QDs, after their morphological transformation occurring during ligand exchange. SAXS data confirm the evolution from multifaceted, spherical-like to more stable cubic-like nanocrystals (Fig. 5b,c) and the subsequent oriented attachment before (or concomitantly to) the binding of the new ligand. In such reconstruction, the dipole–dipole interaction of pristine QDs may bring the nanocrystals in close proximity to each other, favouring the attachment after a minor reorientation[29,30]. In the smallest K_3AsS_4-capped PbS QDs there is no evidence of fusion; however, the evolution towards a more stable cubic-like morphology, with extended {100} facets (Fig. 5b), is observed.

In our OA-capped PbS QDs, simultaneous with the morphological evolution, changes in QD composition, occurring at both the surface and the interior of the nanocrystals, also emerged from the DSE analysis. The QD stoichiometry models used in the DSE analysis are summarized in Fig. 6. A PbS/PbS_x core-shell structure with $x \leq 1$ was initially considered, corresponding to a stoichiometric core and a S-deficient shell (Fig. 6c), following the most accepted model in other works[9,10]. Here, the Pb:S ratio depends on the vacancies of S atoms in the shell. Considering the much simpler spherical PbS_x model in which S deficiency is allowed within the entire QD volume, and comparing the reduced χ^2 of the two models (plotted as a function of α_{RH} in Fig. 6a), we find that the DSE method is sensitive to the region of the nanocrystal where vacancies are located. When we allowed the Pb:S ratio to vary independently within the core and shell (Pb_yS/PbS_x, with $x, y \leq 1$, Fig. 6b), the agreement between the calculated and experimental

data significantly improved for all samples, irrespective of the α_{RH} angle. This finding indicates that the freshly prepared PbS QDs have a Pb-deficient core and a S-deficient shell, both showing a slight size dependence (Supplementary Table 5). Although not totally unexpected (metal vacancies are reported in cation exchange mechanisms[31]), what is surprising in this work is the large concentration of Pb vacancies, which occur in the presence of other structural distortions. This finding closely resembles the case of the isostructural GeSbTe-based phase-change materials, stabilized by the presence of up to 20% cation-site intrinsic defects[32]. Our DFT calculations indicate a significantly reduced vacancy formation energy in the rhombohedrally distorted lattice, because three out of six Pb-S bonds are weakened by the structural deformation. However, under tensile strain, the formation of up to ~10% vacant sites remains energetically favourable (Supplementary Fig. 26), well below the DSE-based results. We attribute such overestimation to the well-known anisotropic and anharmonic distribution of Pb atom displacements[8,33], accounted for neither in powder diffraction analyses nor in our model. Nevertheless, the χ^2 values for the vacancy level indicated by DFT remains markedly lower than for a stoichiometric PbS core (see Supplementary Fig. 28).

Pb vacancies in the core may be driven by a number of concomitant factors related to the QD charge neutrality: the tendency of excess oleate to bind Pb atoms on the surface; the number of surface-bound oleates, which is limited by steric requirements; and the high surface-to-volume ratio of the QDs. More importantly, photoluminescence quantum yields and DFT calculations demonstrate that the structural distortion and a limited amount of Pb vacancies are not detrimental to the photophysical properties (see Supplementary Information for details and further discussion).

The relatively large content of S in the approximately 1-nm-thick QD shell and the relatively low Pb:S ratio of the QDs change significantly on sample oxidation. The results at the optimal α_{RH} angle for each of the three QD sizes, for both pristine and aged QDs, are shown in Fig. 5c,d (see also Supplementary Fig. 7 and Supplementary Table 5). In the pristine case, the calculated total diameter agrees well with estimates from TEM analysis and absorbance spectra (Supplementary Figs 17 and 19). At larger sizes, the S-deficient shell thickens, resulting in slightly lower Pb:S ratios. On oxidation, samples undergo significant modifications culminating in the formation of a Pb-terminated layer, larger Pb:S ratios (Fig. 6c, dashed green line, and Supplementary Table 5) and slightly smaller overall sizes (Fig. 6d and Supplementary Table 4)[10]. The concomitant depletion of Pb in the core and QD size reduction could be attributed to a metal ion migration towards the surface, a vacancy-mediated process invoked in many experimental studies of cation exchange[31]. Assuming that the number of oleates at the QD surface is solely determined by a charge balance mechanism, an average coverage of ~2 and ~4 oleates nm^{-2} is calculated, for fresh and oxidized samples, respectively (Fig. 6c, brown solid and dashed lines), in line with the experimentally determined values for other syntheses[9]. The presence of additional neutral oleic acid molecules or the action of other anionic ligands, which are likely to occur during oxidative post-synthesis changes at the QD surface[11,12], cannot be excluded.

The results presented here shed new light onto the crystal structure of PbE QDs and reshape the understanding of their structural, compositional and morphological properties. These insights highlight the intrinsic complexity of deceptively simple rock-salt structures on extreme downsizing and surface ligand-induced effects, and point to the importance of such studies for the development of QD-based devices.

Methods

Methods and any associated references are available in the online version of the paper.

Received 16 June 2015; accepted 11 May 2016; published online 13 June 2016

References

1. Kovalenko, M. V. *et al*. Prospects of nanoscience with nanocrystals. *ACS Nano* **9,** 1012–1057 (2015).
2. Kovalenko, M. V., Scheele, M. & Talapin, D. V. Colloidal nanocrystals with molecular metal chalcogenide surface ligands. *Science* **324,** 1417–1420 (2009).
3. Ibañez, M. *et al*. Electron doping in bottom-up engineered thermoelectric nanomaterials through HCl-mediated ligand displacement. *J. Am. Chem. Soc.* **137,** 4046–4049 (2015).
4. Zhang, J., Gao, J., Miller, E. M., Luther, J. M. & Beard, M. C. High photocurrent PbSe solar cells with thin active layers. *ACS Nano* **8,** 614–622 (2014).
5. Lan, X., Masala, S. & Sargent, E. H. Charge-extraction strategies for colloidal quantum dot photovoltaics. *Nature Mater.* **13,** 233–240 (2014).
6. Zagorac, D., Doll, K., Schön, J. C. & Jansen, M. Sterically active electron pairs in lead sulfide? An investigation of the electronic and vibrational properties of PbS in the transition region between the rock salt and the α-GeTe-type modifications. *Chem. Eur. J.* **108,** 10929–10936 (2012).
7. Bozin, E. S. *et al*. Entropically stabilized local dipole formation in lead chalcogenides. *Science* **330,** 1660–1663 (2010).
8. Kastbjerg, S. *et al*. Direct evidence of cation disorder in thermoelectric lead chalcogenides PbTe and PbS. *Adv. Funct. Mater.* **23,** 5477–5483 (2013).
9. Moreels, I. *et al*. Size-tunable, bright, and stable PbS quantum dots: a surface chemistry study. *ACS Nano* **5,** 2004–2012 (2011).
10. Moreels, I., Fritzinger, B., Martins, J. C. & Hens, Z. Surface chemistry of colloidal PbSe nanocrystals. *J. Am. Chem. Soc.* **130,** 1581–1586 (2008).
11. Zherebetsky, D. *et al*. Hydroxylation of the surface of PbS nanocrystals passivated with oleic acid. *Science* **344,** 1380–1383 (2014).
12. Anderson, N. C., Hendricks, M. P., Choi, J. J. & Owen, J. S. Ligand exchange and the stoichiometry of metal chalcogenide nanocrystals: spectroscopic observation of facile metal-carboxylate displacement and binding. *J. Am. Chem. Soc.* **135,** 18536–18548 (2013).
13. Kim, D., Kim, D.-H., Lee, J.-H. & Grossman, J. C. Impact of stoichiometry on the electronic structure of PbS quantum dots. *Phys. Rev. Lett.* **110,** 196802 (2013).
14. Cervellino, A., Frison, R., Bertolotti, F. & Guagliardi, A. DEBUSSY 2.0—the new release of a Debye user system for nanocrystalline and/or disordered materials. *J. Appl. Crystallogr.* **48,** 2026–2032 (2015).
15. Chattopadhyay, T., Boucherlet, J. X. & von Schnering, H. G. Neutron diffraction study on the structural phase transition in GeTe. *J. Phys. C* **20,** 1431–1440 (1987).
16. Berger, R. *et al*. Surface stress in the self-assembly of alkanethiols on gold. *Science* **276,** 2021–2024 (1997).
17. Cho, K. S., Talapin, D. V., Gaschler, W. & Murray, C. B. Designing PbSe nanowires and nanorings through oriented attachment of nanoparticles. *J. Am. Chem. Soc.* **127,** 7140–7147 (2005).
18. Klokkenburg, M. *et al*. Dipolar structures in colloidal dispersions of PbSe and CdSe quantum dots. *Nano Lett.* **7,** 2931–2936 (2007).
19. Lee, S. M., Jun, Y. W., Cho, S. N. & Cheon, J. Single-crystalline star-shaped nanocrystals and their evolution: programming the geometry of nano-building blocks. *J. Am. Chem. Soc.* **124,** 11244–11245 (2002).
20. Dong, L., Chu, Y., Zuo, Y. & Zhang, W. Two-minute synthesis of PbS nanocubes with high yield and good dispersibility at room temperature. *Nanotechnology* **20,** 125301 (2009).
21. Huang, W.-C., Lyu, L.-M., Yang, Y.-C. & Huang, M. H. Synthesis of Cu_2O nanocrystals from cubic to rhombic dodecahedral structures and their comparative photocatalytic activity. *J. Am. Chem. Soc.* **134,** 1261–1267 (2012).
22. Simon, P. *et al*. Interconnection of nanoparticles within 2D superlattices of PbS/oleic acid thin films. *Adv. Mater.* **26,** 3042–3049 (2014).
23. Boneschanscher, M. P. *et al*. Long-range orientation and atomic attachment of nanocrystals in 2D honeycomb superlattices. *Science* **344,** 1377–1380 (2014).
24. Matthew, K., Sundararaman, R., Letchworth-Weaver, K., Arias, T. A. & Hennig, R. G. Implicit solvation model for density-functional study of nanocrystal surfaces and reaction pathways. *J. Chem. Phys.* **140,** 084106 (2014).
25. Schapotschnikow, P., van Huis, M. A., Zandbergen, H. W., Vanmaekelberh, D. & Vlugt, T. J. H. Morphological transformations and fusion of PbSe nanocrystals studied using atomistic simulations. *Nano Lett.* **10,** 3966–3971 (2010).
26. Schliehe, C. *et al*. Ultrathin PbS sheets by two-dimensional oriented attachment. *Science* **329,** 550–2936 (2010).
27. Dirin, N. D. *et al*. Lead halide perovskites and other metal halide complexes as inorganic capping ligands for colloidal nanocrystals. *J. Am. Chem. Soc.* **136,** 6550–6553 (2014).
28. Ning, Z. *et al*. Quantum-dot-in-perovskite solids. *Nature* **523,** 324–328 (2015).
29. Li, D. *et al*. Direction-specific interaction control crystal growth by oriented attachment. *Science* **336,** 1014–1018 (2012).

30. van Huis, M. A., Kunneman, L. T., Overgaag, K., Zandbergen, H. W. & Vanmaekelberh, D. Low-temperature nanocrystal unification through rotations and relaxations probed by *in situ* transmission electron microscopy. *Nano Lett.* **10,** 3966–3971 (2010).
31. Casavola, M. *et al*. Anisotropic cation exchange in PbSe/CdSe core/shell nanocrystals of different geometry. *Chem. Mater.* **8,** 3959–3963 (2008).
32. Wuttig, M. *et al*. The role of vacancies and local distortions in the design of new phase-change materials. *Nature Mater.* **6,** 122–128 (2007).
33. Cervellino, A. *et al*. Diffuse scattering from the lead-based relaxor ferroelectric $PbMg_{1/3}Ta_{2/3}O_3$. *J. Appl. Crystallogr.* **44,** 603–609 (2011).

Acknowledgements

F.B. acknowledges University of Insubria for Junior Fellowship Grant 2013, M.V.K. acknowledges the European Union for financial support via FP7 ERC Starting Grant 2012 (Project NANOSOLID, GA No. 306733), D.N.D. thanks the European Union for Marie Curie Fellowship (PIIF-GA-2012-330524) and M.I. thanks AGAUR for her Beatriu i Pinós post-doctoral grant (2013 BP-A 00344). Synchrotron XRPD data were collected at the X04SA-MS Beamline of the Swiss Light Source. M. Döbeli is gratefully acknowledged for taking RBS spectra. Electron microscopy was performed at the Scientific Center for Optical and Electron Microscopy (ScopeM) at ETH Zürich. Computations were performed using the BlueGene/Q supercomputer at the SciNet HPC Consortium provided through the Southern Ontario Smart Computing Innovation Platform (SOSCIP). We thank N. Stadie and J. Mason for reading the manuscript.

Author contributions

A.G., N.M. and M.V.K. formulated the project. D.N.D. and M.I. synthesized the compounds and performed the optical properties characterization. A.C., F.B., R.F., A.G. and N.M. collected and analysed the X-ray total scattering data. F.K. collected and analysed the electron microscopy images. O.V. and E.H.S. performed DFT calculations. A.G. and N.M. wrote the manuscript, with the contribution of all authors.

Additional information

Supplementary information is available in the online version of the paper. Reprints and permissions information is available online at www.nature.com/reprints. Correspondence and requests for materials should be addressed to A.G. or N.M.

Competing financial interests

The authors declare no competing financial interests.

Methods

QD synthesis. We synthesized highly monodisperse PbS and PbSe QDs according to literature methods, with slight modifications. Details are provided in the Supplementary Information and Supplementary Table 1. Briefly, PbS and PbSe QDs were synthesized by reacting lead acetate and oleic acid, followed by addition of bis(trimethylsilyl)sulfide and tri(*n*-butyl)phosphineselenide, respectively.

QD characterization. The size of the PbS and PbSe QDs was determined by combining three different techniques: transmission electron microscopy (TEM), absorption spectroscopy and wide angle X-ray total scattering (WAXS) techniques (through the DSE modelling). TEM images were collected on a FEI Tecnai F30 microscope. Scanning transmission electron microscopy (STEM) images were collected on an aberration-corrected Hitachi HD-2700CS instrument (Fig. 4 and Supplementary Figs 16–17). Visible–near infrared absorption spectra for diluted colloidal solutions in tetrachloroethylene were collected using a Jasco V670 spectrometer, in the range 400–2,000 nm (for PbS) and 1,000–2,000 nm (for PbSe) (Supplementary Figs 19–21). Photoluminescence (PL) spectra and PL quantum yield (QY) measurements were performed on Fluorolog iHR 320 Horiba Jobin Yvon spectrofluorimeter equipped with a InGaAs detector (Supplementary Fig. 22). For PL QY measurements, QDs were excited at 960 nm by a 450W Xenon lamp and using an IR-26 dye molecule as a standard.

Synchrotron X-ray scattering data were collected at the X04SA-MS Powder Diffraction Beamline of the Swiss Light Source of the Paul Scherrer Institut with 22 and 25 keV beam energies in the 0.5°–130° 2θ range (Fig. 1b and Supplementary Figs 7 and 8a).

The composition of the PbS and PbSe QDs was determined by DSE methods (Fig. 5a and c and Supplementary Figs 9b,c and Supplementary Tables 2 and 3) and, for PbS samples only, also by Rutherford backscattering spectrometry (RBS) performed at the ETH laboratory of Ion-Beam Physics (Supplementary Fig. 23 and Supplementary Table 2). The occurrence of crystalline contaminants prevented a meaningful RBS analysis of the PbSe QDs.

Textural effects on PbS and PbSe dried samples were determined using laboratory X-ray powder diffractometry (Fig. 3c–f and Supplementary Figs 13–15). Powder diffraction traces were collected using Cu Kα radiation ($\lambda = 1.5418$ Å) on a Bruker AXS D8 Advance diffractometer, on samples deposited on a silicon monocrystal zero-background sample holder. Following the conventional rules, *hkl*, (*hkl*), [*hkl*] and {*hkl*} notations are used in the main text and figures to indicate: reflection indices, crystallographic planes, directions and sets of facets (or forms), respectively (in the cubic setting). Further details on characterization methods are provided in the Supplementary Information.

DSE method. The DSE method was applied in this work to characterize very small PbS and PbSe nanocrystals (size range 3–8 nm) in colloidal solutions. Debye's formula describes the average differential cross-section of a randomly oriented collection of particles, regardless of their ordered or disordered atomic arrangement. Compared to conventional diffraction techniques, the DSE takes advantage of simultaneously modelling Bragg and diffuse scattering as a function of the distribution of interatomic distances within the nanoparticle, as follows:

$$I(Q) = \sum_{j=1}^{N} f_j(Q)^2 o_j^2 + 2\sum_{j>i=1}^{N} f_j(Q) f_i(Q) T_j(Q) T_i(Q) o_j o_i \frac{\sin(Qd_{ij})}{(Qd_{ij})} \quad (1)$$

where $Q = 2\pi q$, $q = 2\sin\theta/\lambda$ is the length of the reciprocal scattering vector, λ is the radiation wavelength, f_j is the atomic form factor, d_{ij} is the interatomic distance between atoms i and j, and N is the number of atoms in the nanoparticle. In this formula, thermal vibrations (or static disorder) and partial occupancy factors are also taken into account by two atomic, adjustable parameters (T and o). The first summation in equation (1) addresses the contribution of the (zero) distance of each atom from itself, the second summation (the interference term) that of the non-zero distances between pairs of distinct atoms.

The approach we used in this work is based on a new and fast implementation of the Debye equation, which makes use of sampled interatomic distances instead of the original ones, to speed up calculations, as adopted by the Debussy Suite of programs[14]. The DSE method here was applied to determine structure, size, size distribution and stoichiometry of PbS and PbSe QDs from the WAXS pattern collected on their colloidal solutions. Simulations of SAXS signals in the Porod's region (which, owing to the small size of QDs involved, was directly accessible as part of the WAXS pattern) allowed the morphology of the QDs to be inferred. Graphical outcome of the analysis and main results are shown in Figs 1b–d and 6 and Supplementary Fig. 7 (PbS), Supplementary Figs 8 and 9 (PbSe), Supplementary Fig. 18 and Supplementary Tables 2–7. DSE-derived sizes and size distributions of both PbS and PbSe QDs were successfully used to calculate absorption spectra in good agreement with the experimental ones, as shown in Supplementary Fig. 20 and detailed in the Supplementary Information.

The outcome of the analysis in the SAXS region is shown in Fig. 3a,b and Supplementary Figs 11 and 12. Briefly, in the WAXS region, the DSE-based method included generating a population of core-shell nanocrystals in real space for each α_{RH} angle; using the set of interatomic distances in the Debye equation to simulate the reciprocal space scattering pattern; and optimizing the model parameters to fit the experimental data. Aiming at possibly differentiating the inner and the outer portions of the nanocrystals, refinement included the core diameter, the shell thickness, the site occupancy factor of Pb_{core} and S_{shell} atoms, along with the cell edge. Details of the DSE method and the specific core-shell modelling are provided in the Supplementary Information. The observation of isotropic QDs by high-resolution transmission electron microscopy validated this choice of spherical morphology. In this work, we neglected the outer organic oleate (OA) layer which is nearly invisible to X-rays.

***Ab initio* calculations.** DFT simulations were performed using the QuickStep module of the CP2K program suite[34]. Generalized gradients approximation with Perdew–Burke–Ernzerhof functional, molecules-optimized double ζ-valence polarized basis set and Goedecker–Teter–Hutter pseudopotentials at 300 Ry density cutoff were used. A $30 \times 30 \times 30$ A^3 unit cell with a single k-point was used for bulk PbS, and a $50 \times 50 \times 50$ A^3 cell for ~3 nm nanocrystals. All structures were fully relaxed. The dipole moment of the distorted structures was calculated without performing geometry optimization.

Code availability. Debussy Suite is freely available at http://debussy.sourceforge.net.

References

34. VandeVondele, J. *et al*. Quickstep: fast and accurate density functional calculations using a mixed Gaussian and plane waves approach. *Comput. Phys. Commun.* **167,** 103–128 (2005).